International Journal of Thermal Sciences 191 (2023) 108343

Contents lists available at ScienceDirect

International Journal of Thermal Sciences

journal homepage: www.elsevier.com/locate/ijts

Experimental and numerical study on heat transfer and flow characteristics of molten salt nanofluids in spiral-wound tube heat exchanger

Xiaoming Dong, Yuting Wu *, Cancan Zhang, Yuanwei Lu, Chongfang Ma

Key Laboratory of Enhanced Heat Transfer and Energy Conservation, Beijing Key Laboratory of Heat Transfer and Energy Conversion, Beijing University of Technology, Beijing, 100124, China

ARTICLE INFO

Keywords:
Molten salt nanofluids
Spiral-wound tube heat exchanger
Experimental research
Heat transfer

ABSTRACT

Molten salt is one of the most promising heat transfer and thermal energy storage medium for the third-generation solar thermal power generation, and the spiral-wound tube heat exchanger can improve the heat transfer performance of molten salt. In this paper, the flow and heat transfer characteristics of molten salt nanofluids in spiral-wound tubes are experimentally and numerically studied. Molten salt nanofluids and synthetic oil as the heat transfer fluids, the heat transfer performance of them in the spiral-wound tube heat exchanger were studied. The Wilson separation method was used to process the experimental data, and the heat transfer correlation of molten salt nanofluids is obtained through experiments. The heat transfer correlation can be in good agreement with the experimental data, the heat transfer correlation on the molten salt nanofluids side is $Nu = 0.3897Re^{0.4370}Pr^{1/3}$, Re = 4296–8348, Pr = 13–23, and the maximum error is 17.9%. A three-dimensional model of the spiral-wound tube heat exchanger is used to explore the distribution of the pressure, temperature and velocity fields of the molten salt nanofluids. The friction factor correlation on the molten salt nanofluids side is $f = 4.6729Re^{-0.4855}$, Re = 3536–17684, Pr = 13–23 and the maximum error is 12.65%. The heat transfer correlation and resistance correlation of molten salt nanofluids obtained in this paper can contribute to the design of heat exchanger for the third-generation solar thermal power.

1. Introduction

Solar thermal power generation technology has received extensive attention due to high efficiency and sustainability. Energy storage technology is an effective measure to solve the problem of intermittent solar power generation [1–3]. Molten salt can be used in the field of energy storage because of its large heat capacity, low viscosity, low vapor pressure, scholars around the world have paid extensive attention and carried out related research [4–6].

Liu et al. [7] conducted an experimental study on the turbulent heat transfer of molten salt in a circular tube, and obtained the heat transfer correlation of molten salt in the circular tube. Chen et al. [8] conducted an experimental study on the convective heat transfer of Hitec salt in three kinds of transversely corrugated tubes. He et al. [9] explored the convective heat transfer characteristics of ternary salts in shell and tube heat exchangers through experiments. Yang et al. [10] studied the flow and heat transfer characteristics of molten salt in trough solar collectors by numerical simulation. Chen et al. [11] carried out numerical simulation on the convective heat transfer of molten salt mixed in a unilaterally heated horizontal square tube. The results show that under the condition of non-uniform heating, the buoyancy force causes the core area of molten salt flow to be close to the heating surface to form eddy currents, which can enhance the heat transfer effect. Yang et al. [12] studied the heat transfer and flow performance of molten salt in the annular channel with helical coils by numerical simulation. The results show that adding helical coils can effectively enhance the heat transfer of molten salt in the annular channel, but the flow resistance also increased. Du et al. [13] designed a U-shaped tube for the experimental test of the heat transfer characteristics of molten salt in a shell-and-tube heat exchanger in transition flow, and fitted the heat transfer correlation of molten salt. Qiu et al. [14] proposed a baffle rod shell-and-tube heat exchanger configuration applied in the field of concentrated solar thermal power generation, using ternary salt and heat transfer oil as shell-side working fluids for experimental research. He et al. [15] studied the turbulent heat transfer characteristics of molten salt in shell-and-tube heat exchangers with Reynolds numbers ranging from 10, 000 to 91,000 and 11,000 to 27,000 on the tube side and shell side, respectively. The comparison of available correlations for molten salt is

* Corresponding author.
E-mail address: wuyuting1970@126.com (Y. Wu).

https://doi.org/10.1016/j.ijthermalsci.2023.108343
Received 25 October 2022; Received in revised form 1 March 2023; Accepted 22 March 2023
Available online 17 April 2023

in Table 1.

Compared with the conventional shell and tube heat exchanger, the spiral-wound tube heat exchanger has the advantages of compact structure and excellent heat transfer performance. Lu et al. [16] used numerical simulation method to study the effect of geometrical factors such as tube spacing, tube diameter and number of layers on the flow and heat transfer performance of a multi-layer spiral wound tube. Wang et al. [17] developed a calculation model for the design of floating LNG spiral-wound tube heat exchangers, and found that the heat transfer capacity of the heat exchanger decreased with the increase of the swing amplitude. Wang et al. [18] investigated the effect of different arrangement of spacers on the flow and heat transfer performance of wound heat exchangers. Jian et al. [19] surveyed the flow and heat transfer characteristics of elliptical tubes of spiral-wound tube heat exchanger. Abolmaali et al. [20] studied the effects of the first layer tube number, layer number, ratio of longitudinal pitch to tube outer diameter, radial pitch and tube outer diameter on the flow and heat transfer process on the shell side of the spiral-wound tube heat exchanger. Sun et al. [21] studied the operating characteristics of the spiral wound heat exchanger of floating liquefied natural gas, and analyzed the influence of different sloshing angles, sloshing periods and sloshing amplitudes on the pressure drop characteristics of the spiral-wound tube heat exchanger. Lu et al. [22] studied the flow and heat transfer characteristics of the three-layer spiral-wound tube heat exchanger through experiments and numerical simulations. Jian et al. [23] conducted tests on 10 spiral wound heat exchangers to study the influence of structure and working conditions on the heat transfer and flow characteristics at the tube side of spiral wound heat exchanger, and fitted the correlation formula of heat transfer and resistance. Wu et al. [24] used numerical simulation to study the influence of different pipe diameters, pipe spacing and septum thickness on the flow and heat transfer characteristics of spiral-wound tube heat exchangers, and conducted heat transfer experiments on Y-type and K-type spiral-wound tube heat exchangers respectively. Wang et al. [25] conducted experimental and numerical studies on the shell-side heat transfer and flow characteristics of a spiral-wound tube heat exchanger using a two-layer multi-objective optimization of the performance evaluation criteria and maximum field synergy number. Zhang et al. [26–28] studied the heat discharging and natural convection heat transfer performance of coil heat exchanger in a single molten salt tank.

The literature review that the research on the heat transfer characteristics of molten salt nanofluids mainly focuses on the shape of the pipe and the flow and heat transfer characteristics inside the different forms of heat exchangers [29–32]. However, there are few reports on the flow heat transfer characteristics of molten salt nanofluids in the spiral-wound tube heat exchanger. In this paper, the heat transfer and flow characteristics of molten salt nanofluids in a spiral-wound tube heat exchanger are studied by means of experiments and numerical simulations. An experimental platform for convection heat transfer of a molten salt nanofluids -synthetic oil the spiral-wound tube heat exchanger was built to experimentally explore the heat transfer characteristics of molten salt nanofluids in the spiral-wound tube. At the same time, the three-dimensional modeling calculation of the spiral-wound tube heat exchanger is established to explore the distribution of the pressure, temperature and velocity fields of the molten salt nanofluids and the synthetic oil inside the heat exchanger.

2. Experiment setup and data analysis

2.1. The spiral-wound tube heat exchanger

Fig. 1 is a physical diagram and a schematic diagram of the internal structure of the spiral-wound tube heat exchanger. The counter arrangement is adopted. The working fluid on the tube side is high-temperature molten salt nanofluids, and the fluid on the shell side is synthetic oil. The internal winding tubes of the heat exchanger are two layers, each layer is three tubes, the first layer is arranged clockwise, and the second layer is arranged counterclockwise. The specific structural parameters are shown in Table 2.

2.2. Thermophysical properties of molten salt nanofluids and synthetic oil

The molten salt nanofluids used in this experiment is prepared by self-configured in the laboratory. Fig. 2 Shows the thermal property

Table 1
Comparison of available correlations for molten salt.

Authors	Working fluid	Channel configuration	Correlations
Liu et al. [7]	$LiNO_3$	The concentric tubes	$Nu = 0.024Re^{0.807}Pr^{0.331}$ $Nu = 0.024Re^{0.81}Pr^{0.331}\left(\frac{\mu_f}{\mu_w}\right)0.14$ Re = 17,000–45,000, Pr = 12.7–14.7
Chen et al. [8]	Hitec salts	The corrugated tube	$Nu = 0.0733Re^{0.8}Pr^{1/3}\left(\frac{\mu_f}{\mu_w}\right)^{0.14}(1+\frac{2e}{d})^{-11.45}$ Re = 8000–32,000
He et al. [9]	KNO_3–$NaNO_2$–$NaNO_3$	The shell and tube heat exchanger	The shell side: $Nu = 1.61\left(\frac{RePr}{l/d}\right)^{0.63}\left(\frac{\mu_f}{\mu_w}\right)^{0.32}$ Re = 400–2300
Du et al. [13]	Hitec salts	The shell and tube heat exchanger	The shell side: $Nu = 0.0676Re^{0.70413}Pr^{0.4}$ $Nu = 0.05315Re^{0.74208}Pr^{0.4}\left(\frac{\mu_f}{\mu_w}\right)^{0.25}$ Re = 6142–9125, Pr = 19.43–22.33, $\frac{\mu_f}{\mu_w} = 0.64702$–$0.69681$
Qiu et al. [14]	Hitec salts	The rod baffle shell-and-tube heat exchanger	The shell side: $Nu = 0.1133\,(L_b/D_e)^{-0.303}Re^{0.756}Pr^{1\backslash 3}\left(\frac{\mu_f}{\mu_w}\right)^{0.14}$ Re = 2697–12,517, Pr = 14.2–23.3, $\frac{\mu_f}{\mu_w} = 0.86$–$0.93$
He et al. [15]	Hitec salts	The shell and tube heat exchanger	The tube side: $Nu = 0.024Re^{0.8}Pr^{0.3}$ Re = 44,000–91,000, Pr = 2.2–2.8 $Nu = 0.0206Re^{0.8}Pr^{0.3}$ Re = 10,000–19,000, Pr = 6.5–10.0 The shell side: $Nu = 0.0197Re^{0.8}Pr^{0.4}$ Re = 11,000–27,000, Pr = 3.5–4.9

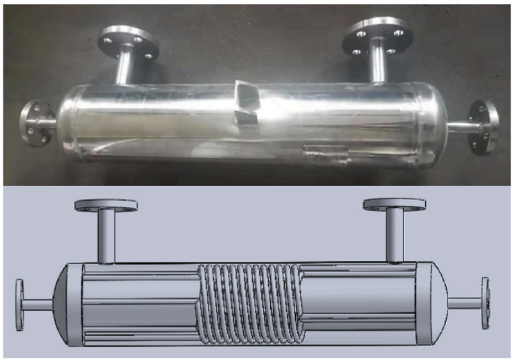

(a)The photo of the spiral-wound tube heat exchanger

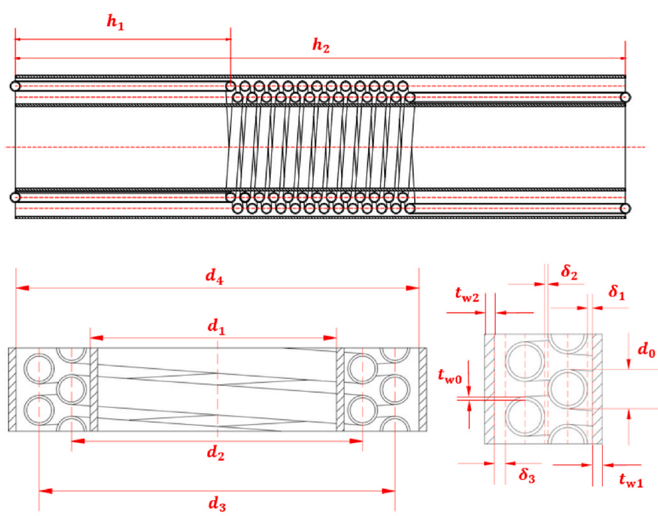

(b) The internal structure of the spiral-wound tube heat exchanger

Fig. 1. The spiral-wound tube heat exchanger.

Table 2
The geometrical parameters of the spiral-wound tube heat exchanger.

Parameter	Value
Bundle straight tube height h_1	225 mm
Bundle height h_2	650 mm
First layer wound tube total length l_1	6237 mm
Second layer wound tube total length l_2	7308 mm
Wound tube outer dimeter d_0-thickness t_{w0}	12 mm/1 mm
Core outer dimeter d_1-thickness t_{w1}	102 mm/3 mm
First layer wound diameter d_2	117 mm
Second layer wound diameter d_3	143 mm
Shell inter dimeter d_4-thickness t_{w2}	162 mm/3 mm
Distance between the core and the first layer δ_1	1.5 mm
Distance between two layers δ_2	1 mm
Distance between the shell and the second layer δ_3	3.5 mm

parameters of molten salt nanofluids and synthetic oil, and ρ, c_p, λ, and μ represent density, specific heat capacity, thermal conductivity, and dynamic viscosity respectively.

2.3. The experiment system

Fig. 3 shows the schematic diagram of the experimental system of the spiral-wound tube heat exchanger, which mainly contains four subsystems including molten salt loop, synthetic oil loop, cooling water loop and data acquisition system. The molten salt loop includes molten salt tank, molten salt pump, heating cable and the circulating pipeline. The

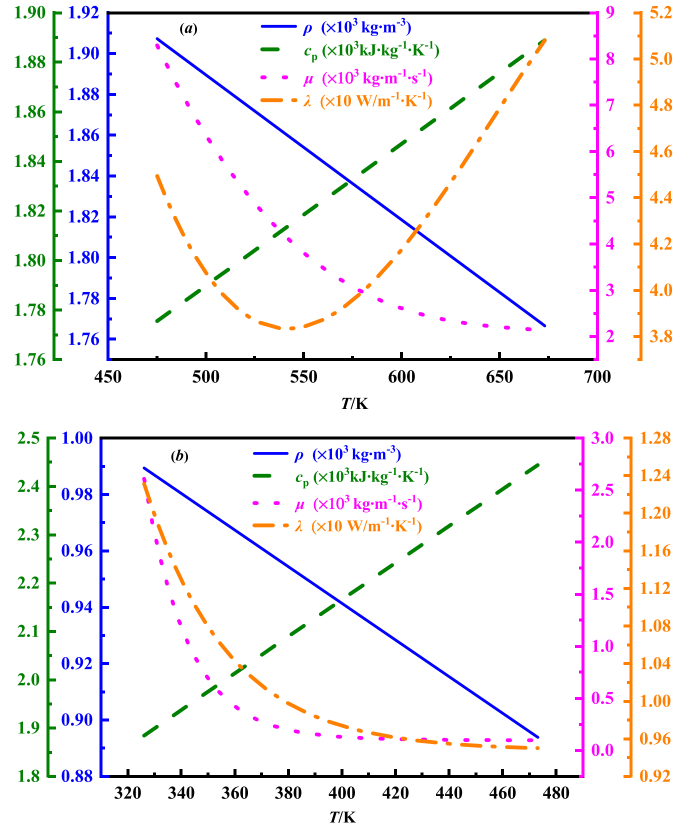

Fig. 2. Thermophysical properties. (a) Molten salt nanofluids (b) Synthetic oil.

high-temperature molten salt tank is mainly used to heat the molten salt, and the molten salt pump transports the molten salt to the tube of the spiral-wound tube heat exchanger. At the same time, thermocouples are arranged at different positions of the pipeline to monitor the change of the outer wall temperature in real time, and the molten salt pipeline is covered with thermal insulation cotton to reduce heat loss. The cooling water loop includes a cooling tower, a circulating water pump and a circulating pipeline, which mainly cools the pump shaft of the high-temperature molten salt pump mentioned above to ensure the normal and stable operation of the molten salt pump. The synthetic oil loop includes a constant temperature synthetic oil tank, a synthetic oil pump, the synthetic oil flowmeter, the synthetic oil cooler and a circulation pipeline, the constant temperature synthetic oil tank is a device used to heat the synthetic oil, and the synthetic oil pump transports the synthetic oil to the shell side of the heat exchanger. The mass flow rate is obtained by a flow meter. In addition, it is necessary to arrange thermocouples at the inlet and outlet of the tube side and the shell side of the spiral-wound tube heat exchanger to monitor the temperature of the molten salt nanofluids and the synthetic oil in real time. In this experiment, the interior of the heat exchanger was preheated with synthetic oil.

2.4. Experimental data analysis

The inlet and outlet temperature of molten salt nanofluids, the inlet and outlet temperature of synthetic oil, and the mass flow of synthetic oil can be directly measured. The mass flow rate of molten salt nanofluids here is obtained by an indirect method and calculated from the heat balance relationship of heat exchanger. For steady-state turbulent convection heat transfer without phase change, the criterion equation can be expressed by Eq. (1)

$$Nu = f(Re, Pr) \tag{1}$$

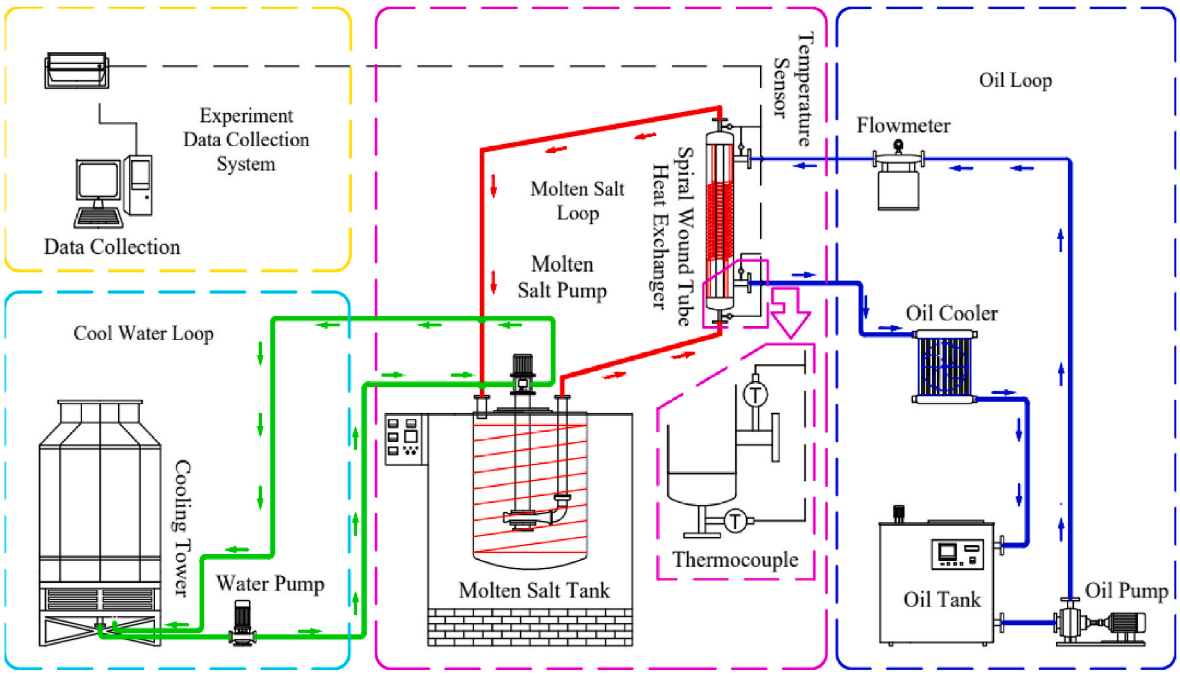

(a) Schematic diagram of the experimental system.

(b) Physical diagram of the experimental system.

Fig. 3. Experimental system of molten salt synthetic oil spiral-wound tube heat exchanger.

where Re is the Reynolds number, Pr is the Prandtl number, which can be measured experimentally or calculated by formulas.

$$Re = \frac{\rho u D}{\mu} \tag{2}$$

where ρ is density, kg•m^{-3}, u is velocity, m•s^{-1}, D represent equivalent diameter, m, μ is dynamic viscosity, kg•m^{-1}•s^{-1}.

For the convenience of calculation, Eq. (1) can be transformed into the following exponential form:

$$Nu = CRe^{N}\,Pr^{M} \tag{3}$$

The values of C, N, and M are constants, and can be obtained by fitting the experimental data.

The molten salt nanofluids mass flow rate is obtained through heat balance calculation as in Eq. (4):

$$m_s = \frac{m_o c_{p,o} \Delta T_o}{c_{p,s} \Delta T_s} \tag{4}$$

where m is mass flow rate, kg•s^{-1}, c_p is specific heat, J•kg^{-1}•k^{-1}, ΔT is inlet and outlet temperature difference, K. The subscripts s and o represent molten salt nanofluids and synthetic oil, respectively.

The total heat transfer coefficient (U) of the heat exchanger can be obtained by the following Eq. (5):

$$U = \frac{Q}{A \Delta T_m} \tag{5}$$

$$Q = m_o c_{p,o} \Delta T_o = m_s c_{p,s} \Delta T_s \tag{6}$$

$$\Delta T_m = \frac{(\Delta T_{max} - \Delta T_{min})}{\ln \frac{\Delta T_{max}}{\Delta T_{min}}} \tag{7}$$

$$\Delta T_{max} = \max(\Delta T_o, \Delta T_s) \tag{8}$$

$$\Delta T_{\min} = \min(\Delta T_o, \Delta T_s) \tag{9}$$

where U is the total heat transfer coefficient, $W \bullet m^{-2} \bullet K^{-1}$, A is the heat transfer area, m^2, ΔT_m is logarithmic mean temperature difference, K.

The relationship between the total heat transfer coefficient of the heat exchanger and the respective heat transfer coefficients of the fluids on both sides is as follows:

$$\frac{1}{U} = \frac{1}{h_s} + \frac{A_{in}}{2\pi\lambda_w L} ln\frac{d_{out}}{d_{in}} + \frac{A_{in}}{h_o A_{out}} \tag{10}$$

where d_{in} and d_{out} are the inner and outer diameters of the tube, respectively, m, h is the heat transfer coefficient, $W \bullet m^{-2} \bullet K^{-1}$.

In each experimental condition, the mass flow rate of the synthetic oil is constant, so it can be considered that the heat transfer coefficient on the synthetic oil side remains unchanged. So it is only necessary to solve the heat transfer coefficient on the molten salt nanofluids side from Eq. (10). The data processing method is Wilson separation method [33], which is a commonly used solution method in the analysis of fluid heat transfer on both sides of the heat exchanger. It can directly separate the convective heat transfer coefficient of the fluid on the other side by changing the total heat transfer coefficient of the heat exchanger and changing the mass flow rate of the fluid on one side.

When the molten salt nanofluids is in the fully developed turbulent stage, the relationship between its convective heat transfer coefficient h_s and flow velocity u_s can be expressed as Eq. (11):

$$h_s = C_s u_s^Y \tag{11}$$

From Eq. (10) and (11), the following relationship can be obtained:

$$\frac{1}{U} = \frac{1}{C_s u_s^Y} + \frac{A_{in}}{2\pi\lambda_w L} \ln\frac{d_{out}}{d_{in}} + \frac{A_{in}}{h_o A_{out}} = A\left(\frac{1}{u_s}\right)^Y + B \tag{12}$$

Among them, A, B, Y are constants, and can be obtained by fitting the experimental data $1/u_s$ and $1/U$. At the same time, h_s can be calculated, and then the experimental value of Nu can be calculated according to the experimental operating condition. The heat transfer correlation can be obtained by fitting the Nu and Re.

The uncertainty analysis method described in Ref. [34] was adopted in this study. If the variable (R) is a function of independent variables X_1, X_2, ..., X_n as shown in Eq. (13), then the relative uncertainty of R is calculated by Eq. (14). The calculated relative uncertainties of Q, $m_{s,in}$, and U are within 2.96%, 3.77%, and 3.26%, respectively. The detailed uncertainties of the measured and calculated parameters are presented in Table 3.

$$R = f(X_1, X_2, \ldots, X_n) \tag{13}$$

$$\frac{\delta_R}{R} = \frac{\sqrt{\left(\frac{\partial R}{X_1}\delta_{X_1}\right)^2 + \left(\frac{\partial R}{X_2}\delta_{X_2}\right)^2 + \ldots + \left(\frac{\partial R}{X_n}\delta_{X_n}\right)^2}}{R} \tag{14}$$

where δ_{X_i} is the uncertainty of variable X_i.

Table 3
Uncertainty of direct and indirect measurements.

	Parameter	Range	Uncertainty
Measurements	$m_{o,in}$ ($kg \bullet s^{-1}$)	2.35–2.37	±1.20%
	$T_{s,in}$ (K)	561–614	±0.20%
	$T_{o,in}$ (K)	394–416	±0.20%
	$T_{s,out}$ (K)	536–571	±0.20%
	$T_{o,out}$ (K)	405–429	±0.20%
Calculated value	$m_{s,in}$ ($kg \bullet s^{-1}$)	0.63–1.47	±3.77%
	Q (kW)	39.44–69.18	±2.96%
	U ($W \bullet m^{-2} \bullet K^{-1}$)	686.94–1344.90	±3.26%

3. Numerical simulation

3.1. Numerical model and model validation

In order to obtain the flow and heat transfer characteristics of molten salt nanofluids and synthetic oil in the spiral-wound tube heat exchanger, that is, the changes of the physical fields such as the temperature field and pressure field of the working medium, and the correlation of the pressure drop of the molten salt nanofluids in the spiral-wound tube, a numerical simulation study was carried out.

Based on the actual flow and heat transfer process of the working fluid in the spiral-wound tube heat exchanger, the following assumptions are made in the process of numerical modeling. The fluid is incompressible, and the physical property changes of the fluid during the heat exchange process can be ignored, and the medium gravity cannot be ignored. The heat loss between the spiral-wound tube heat exchanger and the environment can be ignored, and the contact surface between the fluid. And the wall is a non-slip boundary. In this paper, the ANSYS Fluent is used to numerically simulate the flow and heat transfer characteristics of the working fluid in the spiral-wound tube heat exchanger.

Continuity equation:

$$\frac{\partial}{\partial x_i}(\rho u_i) = 0 \tag{15}$$

Momentum equation:

$$\frac{\partial}{\partial x_i}(\rho u_i u_k) = \frac{\partial}{\partial x_i}\left(\mu\frac{\partial u_k}{\partial u_i}\right) - \frac{\partial P}{\partial x_k} \tag{16}$$

Energy equation:

$$\frac{\partial}{\partial x_i}(\rho u_i T) = \frac{\partial}{\partial x_i}\left(\frac{\lambda}{c_p}\frac{\partial T}{\partial x_i}\right) \tag{17}$$

The internal structure of the spiral-wound tube heat exchanger studied in this paper is relatively complex, and the curvature of the flow channel changes greatly. The calculation results obtained by different turbulence models may be different. Therefore, it is necessary to compare the calculation results of different turbulence models with the experimental results to ensure that the calculated results of the selected turbulence model are closer to the actual values. The commonly used turbulence model for simulating the flow of working fluid in heat exchangers is the k-ε model, and there are three k-ε models in the fluent software: standard k-ε model, RNG k-ε model, standard Realizable k-ε model. In order to verify the accuracy of the above three turbulence models, the three models were used to simulate a specific heat exchange condition, and the deviation between the outlet temperature of the molten salt nanofluids and synthetic oil on both sides and the experimental results was used as the evaluation index. The comparison results are shown in Table 4, and it can be seen that the calculation results of the Realizable k-ε model are the closest to the experimental values, so Realizable k-ε model is adopted.

k equation:

$$\frac{\partial}{\partial x_i}(\rho k u_i) = \frac{\partial}{\partial x_j}\left(\left(\mu + \frac{\mu_t}{\sigma_k}\right)\frac{\partial k}{\partial x_j}\right) + G_k - \rho\varepsilon \tag{18}$$

ε equation:

Table 4
Model validation.

	Exp.	Standard $k-\varepsilon$	RNG $k-\varepsilon$	Realizable $k-\varepsilon$
$T_{s,out}$ (K)	539.33	536.90	537.64	538.33
Error (%)		0.45	0.31	0.19
$T_{o,out}$ (K)	410.02	410.38	410.14	409.96
Error (%)		0.09	0.03	0.01

$$\frac{\partial}{\partial x_i}(\rho \varepsilon u_i) = \frac{\partial}{\partial x_j}\left(\left(\mu + \frac{\mu_t}{\sigma_\varepsilon}\right)\frac{\partial \varepsilon}{\partial x_j}\right) + \rho C_1 S_\varepsilon - \rho C_2 \frac{\varepsilon^2}{\kappa + \sqrt{\vartheta\varepsilon}} \tag{19}$$

where $C_1 = \max\left[0.43, \frac{\eta}{\eta+5}\right]$, $\eta = S\frac{\kappa}{\varepsilon}$, $S = \sqrt{2S_{ij}S_{ij}}$, $S_{ij} = 0.5\left(\frac{u_i}{x_j} + \frac{u_j}{x_i}\right)$, $C_\mu = \mu_t S^2$, $C_2 = 1.9$, $\sigma_k = 1.0$, $\sigma_\varepsilon = 1.2$, G_k represents the effect of velocity gradient on first-order turbulent kinetic energy, and C_μ is a function of average tension, rotational velocity, and angular velocity.

The coupling pressure and velocity are solved by SIMPLE algorithm. The energy equation and momentum equation both use a second-order scheme, and both the turbulent kinetic energy and the turbulent dissipation use a first-order scheme. The convergence criteria for each governing equation is that all residual targets are set to 10^{-6}. The mesh grid of the spiral-wound tube heat exchanger is shown in Fig. 4.

The density of the grid has a great influence on the accuracy of the numerical simulation results, and it is necessary to verify the grid independence. The models with different grid numbers are calculated respectively, and the outlet temperature of the working fluid on both sides is used as the evaluation index. The calculation results are shown in Table 5. It can be seen that when the number of grids is greater than 23.93 million, the change of outlet temperature of fluids on both sides is less than 0.07%. Considering the calculation cost, 23.93 million grids are selected for all calculations.

3.2. Boundary conditions

Since the heat exchange between molten salt nanofluids and synthetic oil in the spiral-wound tube heat exchanger belongs to single-phase heat exchange, it is not necessary to select other models except the energy equation and turbulence model. Both molten salt nanofluids and synthetic oil adopt inlet mass flow rate boundary, the mass flow rate and temperature of molten salt nanofluids inlet are 0.8 $kg \cdot s^{-1}$ and 597 K respectively, and the inlet mass flow rate and inlet temperature of synthetic oil are 2.35 $kg \cdot s^{-1}$ and 404 K respectively. The outlet boundary is set as the pressure outlet, and the wall of heat exchanger is set as the coupling wall surface without slippage, and the wall material is stainless steel with a thickness of 1 mm. And diabatic boundary conditions for other surfaces. During the experiment, the shell of the heat exchanger is wrapped with multi-layer insulation cotton, which can effectively reduce the heat dissipation loss. Therefore, it is practical to use an insulating wall for the heat exchange exterior. The simulation calculation method is set to steady-state calculation.

Table 5
Grid independence verification.

	Grid number ($\times 10^4$)			
	1928	2061	2393	3658
$T_{s,out}(K)$	538.16	537.94	538.33	538.74
$T_{o,out}(K)$	409.98	410.05	409.96	409.84

4. Results and discussions

4.1. Analysis of experiment results

Fig. 5 shows the relationship between the convective heat transfer coefficient on the molten salt nanofluids side and the value of *Re*. Under the existing conditions in the laboratory, the molten salt nanofluids Reynolds number varies from 4500 to 8000. When the temperature of the synthetic oil side is constant, the convective heat transfer coefficient of the molten salt side decreases by 15–19.4% as the temperature of the molten salt increases from 573 K to 613 K. At the same time, it can be seen that when the temperature and flow rate of molten salt are constant, the heat transfer coefficient of molten salt side decreases gradually with the increase of the temperature of synthetic oil side. It also can be clearly seen that with the increase of *Re*, the convective heat transfer coefficient on the molten salt nanofluids side increases continuously, indicating that the molten salt nanofluids gradually develops from transitional flow to vigorous turbulent flow, and heat transfer is strengthened. It can also be seen that as the temperature of the molten salt nanofluids increases, the heat transfer coefficient is decreases on the molten salt nanofluids side. The heat transfer coefficient on the molten salt nanofluids side decreases with the increase of the molten salt nanofluids inlet temperature. In addition, it can be seen from the figure that with the increase of the synthetic oil, the heat transfer coefficient of the molten salt nanofluids side gradually decreases. This may be because the inlet temperature of molten salt rises, making the temperature difference between the inlet and outlet of molten salt less than the outlet temperature difference of synthetic oil in the whole heat exchanger process. In the process of data processing in this experiment, the mass flow rate of molten salt is calculated according to the heat balance, so that the mass flow rate calculated by molten salt decreases with the increase of molten salt inlet temperature, so the heat transfer coefficient of molten salt side also decreases with the increase of molten salt inlet temperature. The synthetic oil pump used in this experiment is a

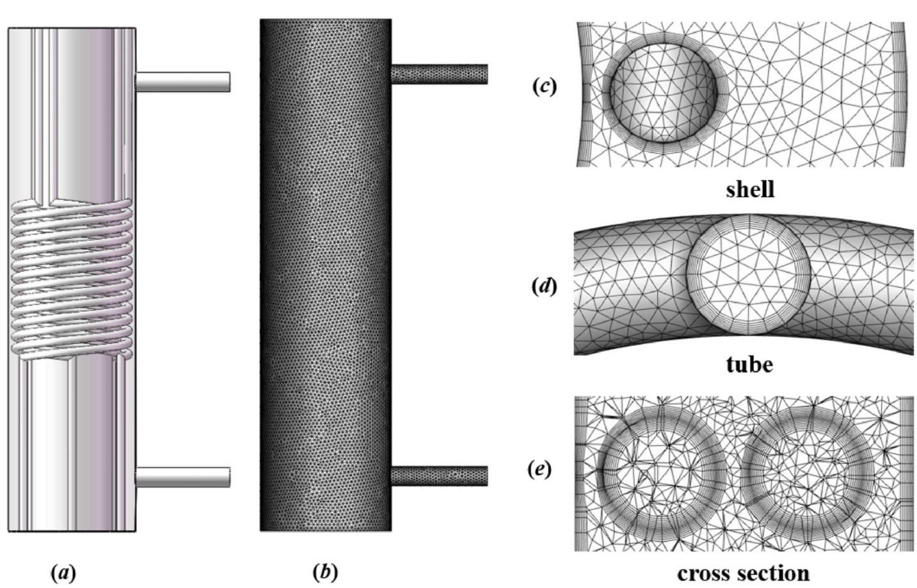

Fig. 4. Mesh division of heat exchanger.

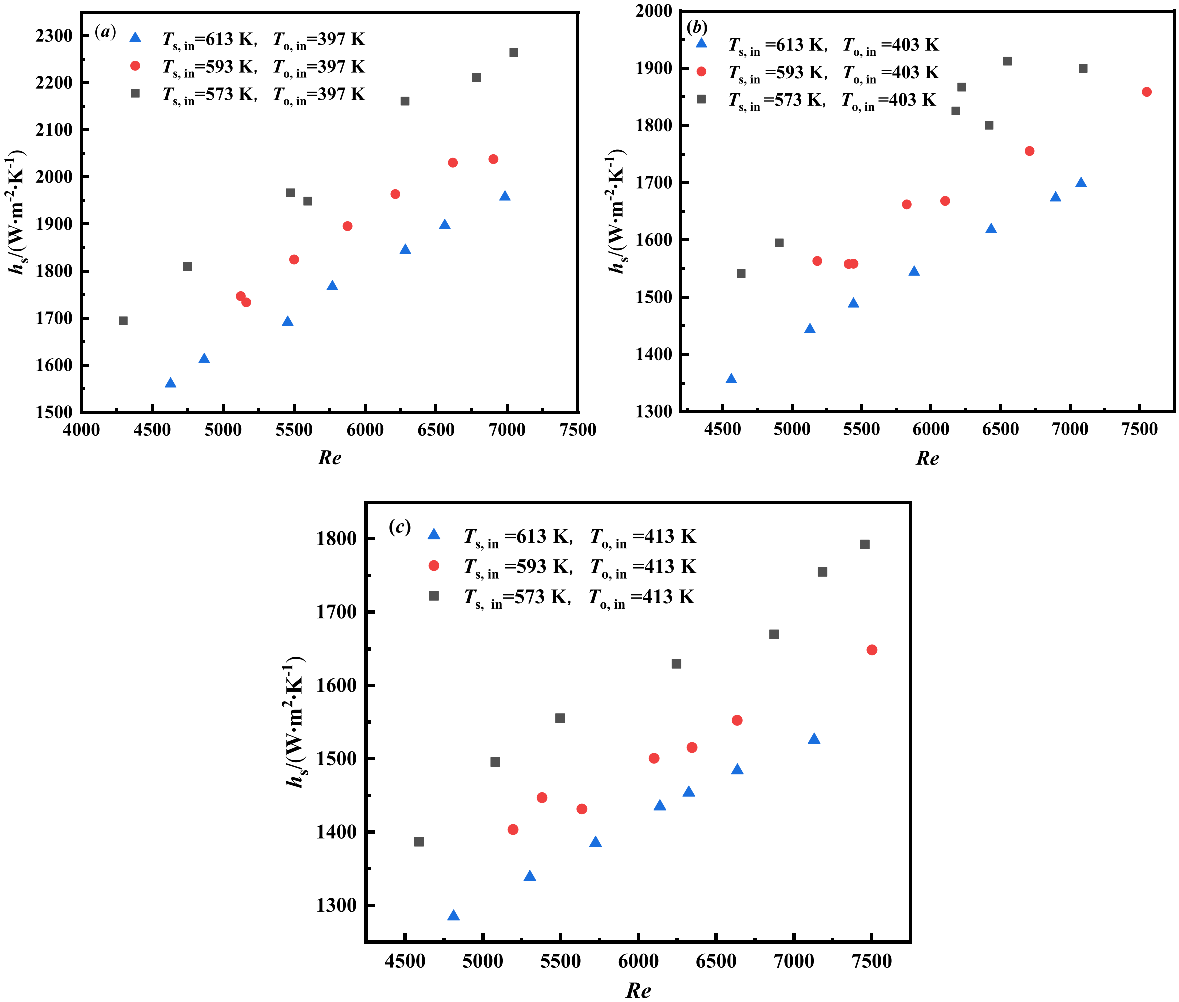

Fig. 5. Variation of heat transfer coefficient on molten salt nanofluids side with Reynolds number.

constant speed pump, so it can be considered that the flow rate of synthetic oil is constant in the range of experimental conditions. This may be because the inlet temperature of synthetic oil rises, so that the heat exchange temperature difference between hot and cold working medium decreases, and the inlet and outlet temperature difference between heat exchange and cold and hot working medium also decreases. Therefore, the calculated value of molten salt mass flow decreases, so the heat transfer coefficient of molten salt side decreases with the increase of inlet temperature of synthetic oil.

Fig. 6 Shows the total heat transfer coefficient varies the Reynolds number on molten salt nanofluids side. It can be roughly seen that the total heat transfer coefficient of the heat exchanger increases with the increase of the Re on the molten salt nanofluids side. When the temperature of the synthetic oil side is constant and the temperature of molten salt is between 573 and 613 K, the total heat transfer coefficient does not change significantly, and when the Reynolds number is from 4500 to 7500, the total heat transfer coefficient changes by 800–1000 W m^{-2} K^{-1}. When the temperature of molten salt is constant at 613 K, the total heat transfer coefficient increases by 11.7% when the temperature of synthetic oil increases from 373 to 413 K. The temperature is independent, indicating that the heat transfer on the molten salt nanofluids side is effectively enhanced in the process of developing from transitional flow to vigorous turbulent flow. It can be seen from the above figure that within the range of the Re on molten salt nanofluids side in this experiment, when the inlet temperature of molten salt nanofluids changes, the total heat transfer coefficient of the heat exchanger does not show a significant difference. This may be caused by the higher the inlet temperature of molten salt, the heat transfer temperature difference between the two kinds of working medium will increase, resulting in the total heat transfer and logarithmic average temperature difference of the heat exchanger will increase, so that the change of the total heat transfer coefficient is not obvious. Finally, it can be seen from the figure above that, within the range of molten salt Reynolds number in this experiment, the higher the inlet temperature of synthetic oil is, the greater the total heat transfer coefficient is. Due to the higher the synthetic oil inlet temperature is, the heat transfer temperature difference between the working medium decreases, so the decrease of heat transfer and logarithmic average temperature difference are reduced, but the decrease of heat transfer is less than the logarithmic average temperature difference, so that the total heat transfer coefficient of the heat exchanger increases with the increase of synthetic oil inlet temperature.

Based on the above experimental results, the convective heat transfer relationship of molten salt nanofluids inside the coiled pipe was fitted within the range of the experimental molten salt nanofluids Reynolds number.

Fig. 7 shows the results of experiment and numerical simulation, and found that the results of experiment and numerical simulation are basically consistent. Other numerical simulation results are analyzed in Section 4.2 below.

$$Nu = 0.3897 Re^{0.4370}\ Pr^{1/3} \tag{20}$$

where Re = 4296–8348, Pr = 13–23. It can be seen that the error range of the fitting results is ±20% is acceptable in engineering.

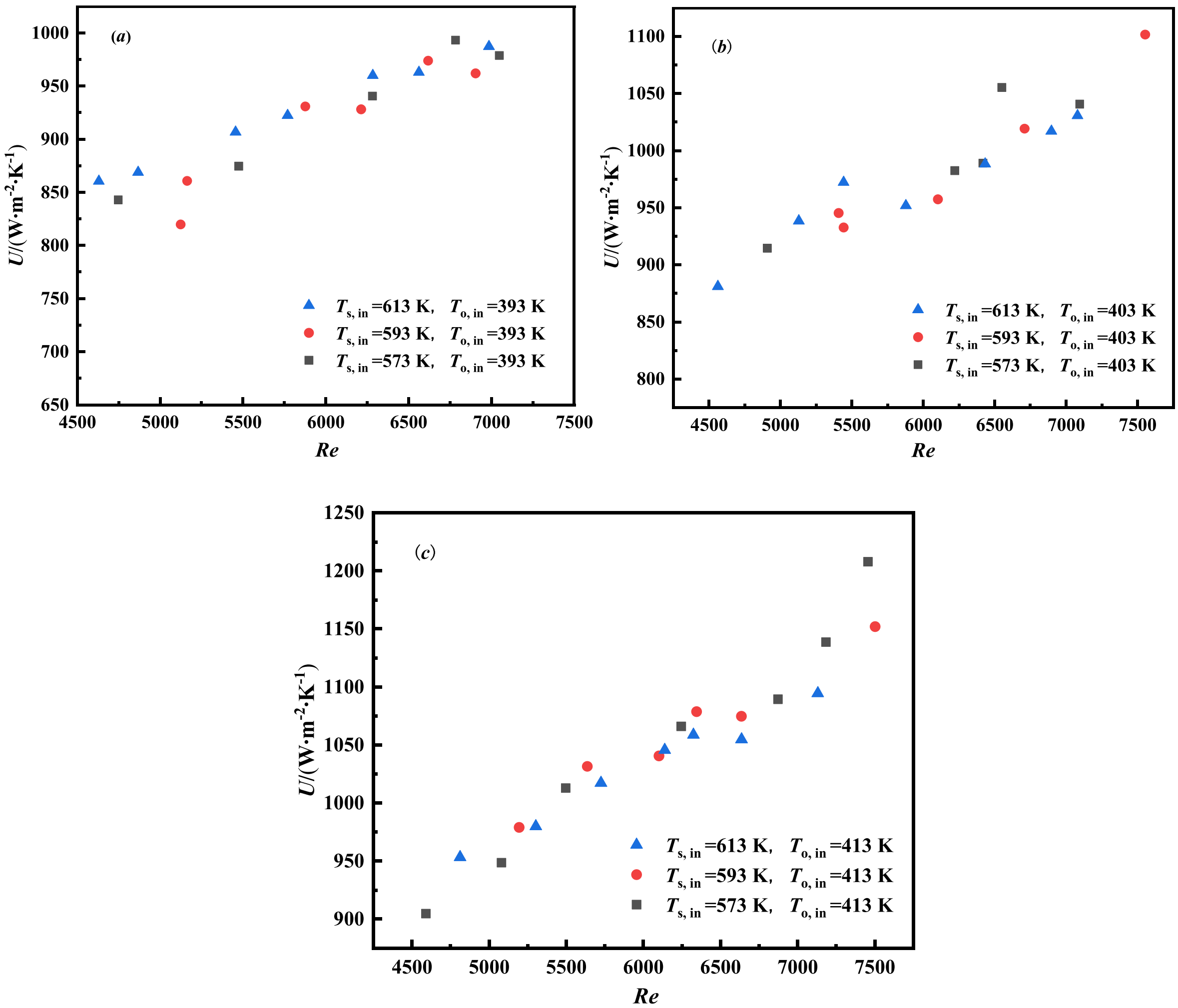

Fig. 6. Variation of total heat transfer coefficient with molten salt nanofluids Reynolds number.

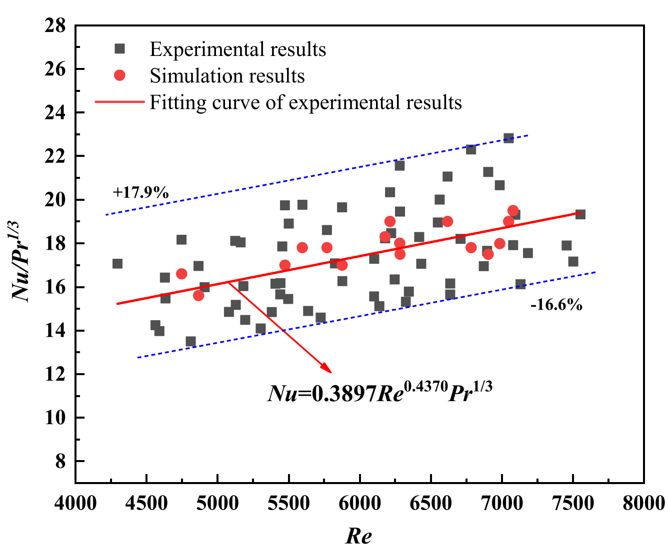

Fig. 7. Heat transfer correlation for molten salt nanofluids.

The reason for the degree of dispersion of the experimental points is slightly larger is that the heat flux density of the heat exchanger is too large during the use of the synthetic oil, which will cause the phase change of some synthetic oil to have a certain impact on the experimental results. In order to minimize the problem of local phase change of the synthetic oil during the heat exchange process, in the improvement of the experimental bench in the later stage, it can be considered to appropriately increase the pressure of the system and increase the phase change temperature of the synthetic oil.

4.2. Analysis of numerical simulation results

Fig. 8 shows the flow and temperature field of molten salt nanofluids in spiral-wound tube heat exchanger. The section on the right in the figure is the longitudinal section of the spiral-wound tube bundle. In order to show the local pressure, temperature and velocity more clearly, one of the inner and outer layers of the tube bundle is selected for analysis and discussion. It can be seen that the distribution of the pressure field, temperature field and velocity field of the molten salt nanofluids in the spiral tube is not uniform, showing a relatively obvious layering phenomenon. There are two main reasons, on the one hand, the pipeline is spiral, and when molten salt nanofluids flows in the pipeline, it will be affected by centrifugal force to generate a secondary flow. On the other hand, due to the continuity of the fluid, the fluid closer to the outside of the tube will flow longer in unit time, so the fluid outside the tube has a faster flow rate, and the inside of the tube is just the opposite. As a result, the heat transfer capacity of the spiral tube is improved.

Fig. 9 shows the flow field and temperature field of molten salt nanofluids on a horizontal cross-section at half the height of the tube bundle in the heat exchanger. It can also be seen from the figure that the physical parameters of the molten salt nanofluids have obvious

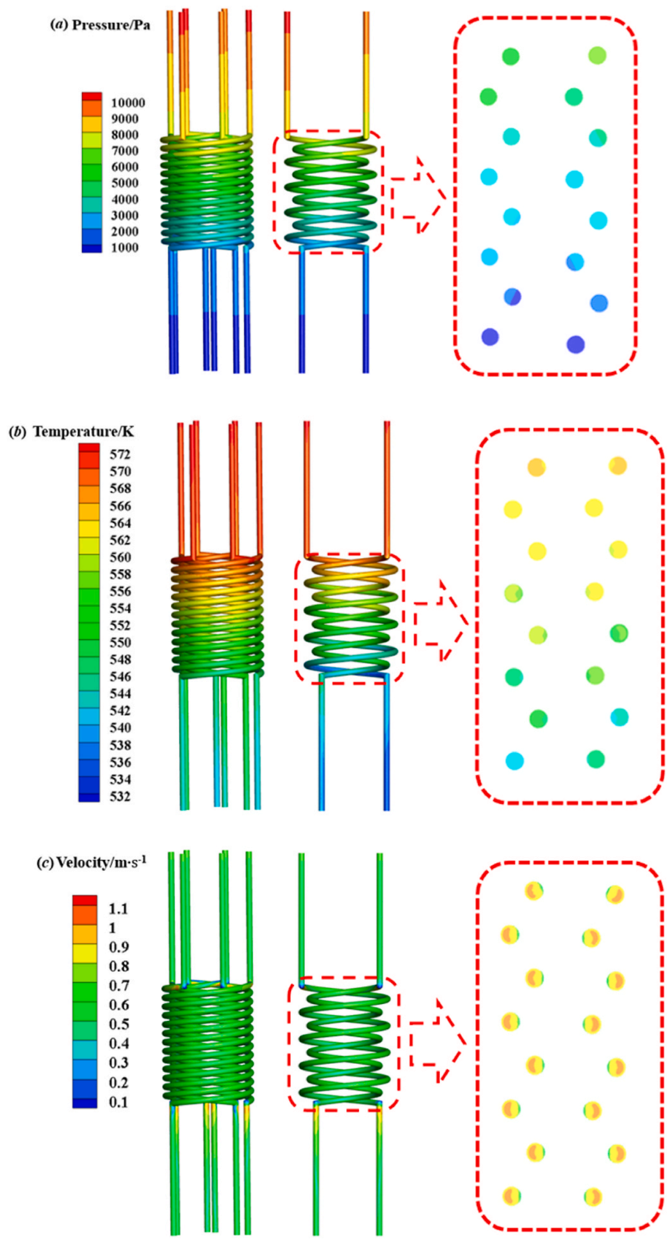

Fig. 8. Flow field and temperature field of molten salt nanofluids in spiral-wound tube heat exchanger.

stratification.

Fig. 10 Shows the flow and temperature field of the synthetic oil in the shell side. The section in the figure is a longitudinal section on the shell side of the spiral-wound tube heat exchanger. It can be seen from Fig. 10(a) that since the synthetic oil flows through the spiral-wound tube bundle, the pressure of the synthetic oil from top to bottom is constantly decreasing. It can be seen from the cross-sectional temperature distribution cloud diagram in Fig. 10(b) that the temperature of the synthetic oil is higher near the inner side of the heat exchanger. The distance between the inner core of the heat exchanger and the first layer of tubes is smaller than the distance between the outer shell and the last layer of tubes, and the flow area of the outer synthetic oil is larger than that of the inner side, so more synthetic oil will flow from the outside, making the outer synthetic oil flow. The temperature is relatively lower inside. It can be seen from the cross-sectional velocity distribution cloud diagram in Fig. 10(c) that the flow rate of the synthetic oil on the outside is faster than that on the inside, which is consistent with the above results. At the same time, it can be seen that after the synthetic oil flows through the tube bundle, a flow stagnation area appears on the back of the tube. It can be seen from the cross-sectional velocity distribution diagram in Fig. 10(c) that the flow rate of the heat transfer oil on the outside is faster than that on the inside, which also verifies the above results. At the same time, it can also be seen that after the heat transfer oil flows through the tube bundle, a flow stagnation area appears on the back of the spiral-wound tube, which is an inevitable phenomenon when the fluid flushes the tube bundle. Therefore, the structural optimization of the heat exchange tube is an effective means to reduce the flow dead zone in the heat exchange area.

The molten salt nanofluids pressure drop value obtained by numerical simulation is processed, and the relationship between the molten salt nanofluids Reynolds number and the resistance coefficient is obtained by fitting. The results are shown in Fig. 11:

$$f = 4.6729Re^{-0.4855} \tag{21}$$

where Re = 3536–17,683, It can be seen that the error range of the fitting results is ±15% is acceptable in engineering.

5. Conclusions

In this paper, the spiral-wound tube heat exchanger is taken as the research object, and the molten salt nanofluids and synthetic oil are used as heat transfer fluid to carry out experiments and numerical simulation studies respectively. The experiment was carried out with the salt-side temperature ranging from 573 K to 613 K, mass flow rate ranging from 0.6 to 1 kg/s. The corresponding Reynold's number range is Re = 4296–8348. The flow heat transfer characteristics inside the heat exchanger, the following results are obtained:

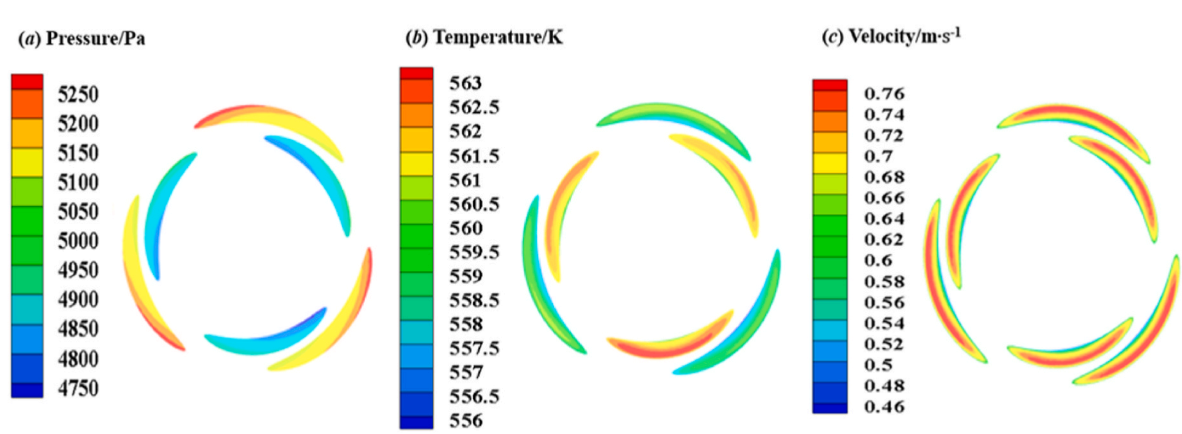

Fig. 9. Flow field and temperature field of molten salt nanofluids on a horizontal cross-section in the heat exchanger.

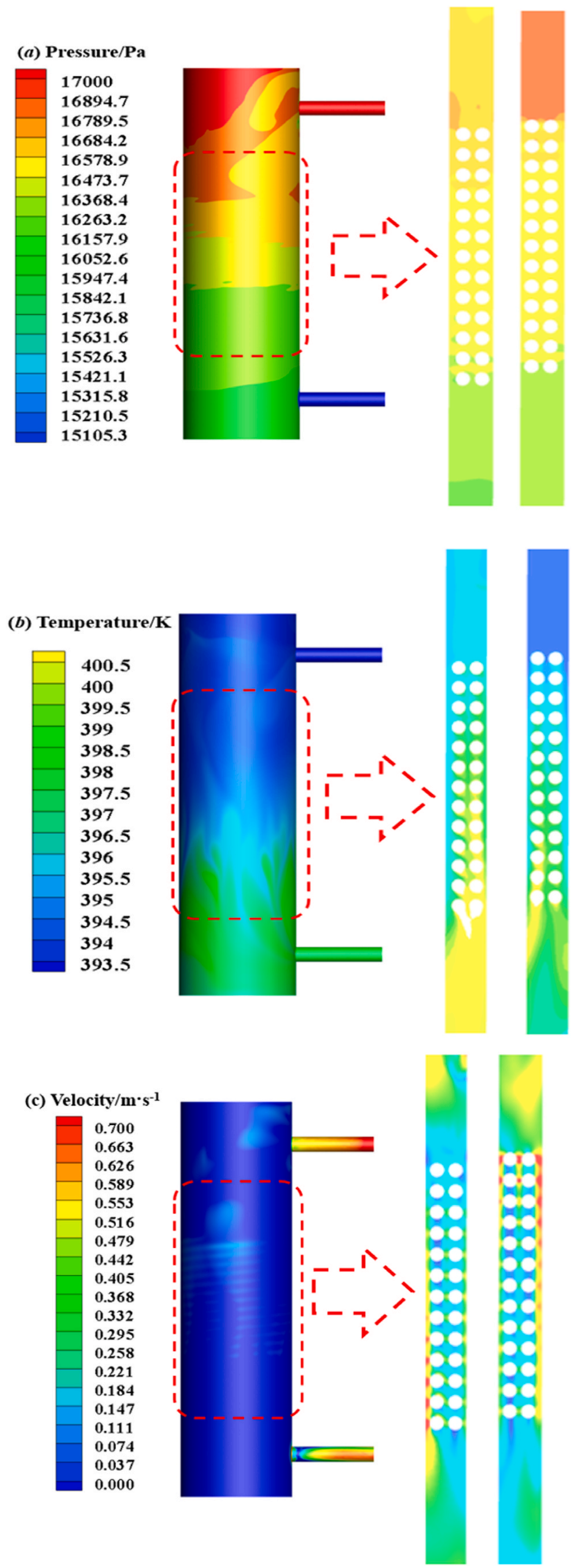

Fig. 10. Flow field and temperature field of the synthetic oil in the shell side.

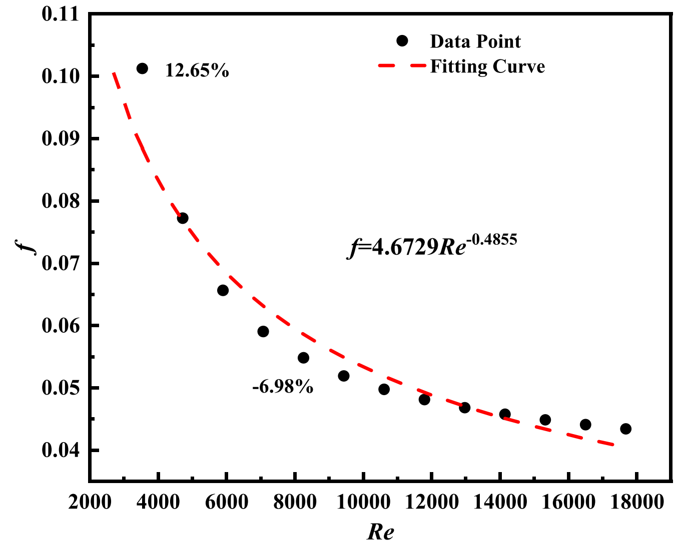

Fig. 11. Friction factor correlation for molten salt nanofluids.

(1) Using the Wilson separation method to process the temperature data of the inlet and outlet of the working fluid, the heat transfer correlation on the molten salt nanofluids side is $Nu = 0.3897Re^{0.4370}Pr^{1/3}$, Re = 4296–8348, Pr = 13–23. The maximum fitting error is 17.9%, which belongs to the allowable error range of the project. The experimental results are more accurate and reliable.
(2) The numerical simulation calculation results that the pressure, temperature and velocity field distribution of molten salt nanofluids and synthetic oil in the spiral-wound tube heat exchanger are not uniform. The main reason is that the special geometric structure of the spiral-wound tube makes the working medium in the tube undergo centrifugal force during the flow to generate a secondary flow, which makes the disturbance more intense and enhances heat transfer. The flow channel structure on the shell side is more complex. After the working fluid flows through the tube bundle, a certain flow dead zone will be formed on the back of the tube bundle, so the physical field distribution will change accordingly.
(3) The accuracy of the numerical simulation is verified by the experimental results, and the pressure value of the molten salt nanofluids inlet and outlet calculated by the numerical simulation is processed. The friction factor correlation on the molten salt nanofluids side is $f = 4.6729Re^{-0.4855}$, Re = 3536–17684, Pr = 13–23 and the maximum error is 12.65%.

The heat transfer correlations developed in this paper have good agreements with experimental data, which can contribute to the design of heat exchanger for the third-generation solar thermal power.

Declaration of competing interest

The authors declare that they have no known competing financial interests or personal relationships that could have appeared to influence the work reported in this paper.

Data availability

No data was used for the research described in the article.

Acknowledgments

This work is supported by National Natural Science Foundation of

China (NSFC) (51906003), Science and technology general project of Beijing Municipal Education Commission (KM202210005016), Inner Mongolia Science and Technology Major Project (No. 2021SZD0036).

Nomenclature

A	heat transfer area
d	Diameter, m
d_0	wound tube outer dimeter, m
d_2	first layer wound diameter, m
d_4	shell inter dimeter, m
h	convective heat transfer coefficient $W{\cdot}m^2{\cdot}K^{-1}$
h_2	bundle height, m
L	Length, m
l_2	second layer wound tube total length, m
Nu	Nusselt number
Q	heat load, W
T	temperature, K
ΔT_m	logarithmic mean temperature, K
t_w	thickness of wall, m
U	total heat transfer coefficient $W{\cdot}m^{-2}{\cdot}K^{-1}$

Greek symbols

λ	thermal conduction, $W{\bullet}m^{-1}{\cdot}K^{-1}$
μ	dynamic viscosity, $kg{\bullet}m^{-1}{\cdot}s^{-1}$
δ_1	distance between the core and the first layer, m
δ_3	distance between the shell and the second layer, m

Subscript

in	inlet
o	oil
w	wall
c_p	specific heat, $J{\cdot}kg^{-1}{\cdot}K^{-1}$
D	equivalent diameter, m
d_1	core outer dimeter, m
d_3	second layer wound diameter, m
H	Hight, m
h_1	bundle straight tube height, m
k	turbulent kinetic energy
l_1	first layer wound tube total length, m
m	mass flow rate, $kg{\cdot}s^{-1}$
Pr	Prandlt number
Re	Reynolds number
ΔT	temperature difference K
t	thickness, mm
u	Velocity, $m{\cdot}s^{-1}$
ρ	density, $kg{\cdot}m^{-3}$
ε	dissipation of turbulent kinetic energy
δ_2	distance between two layers, m
out	outlet
s	molten salt nanofluids

References

[1] Z. Yang, S.V. Garimella, Molten-salt thermal energy storage in thermoclines under different environmental boundary conditions, Appl. Energy 87 (11) (2010) 3322–3329.

[2] T. Bauer, N. Pfleger, D. Laing, et al., High-Temperature Molten Salts for Solar Power Application, Molten Salts Chemistry, 2013, pp. 415–438.

[3] X. Ju, C. Xu, G.S. Wei, et al., A novel hybrid storage system integrating a packed-bed thermocline tank and a two-tank storage system for concentrating solar power (CSP) plants, Appl. Therm. Eng. 92 (2016) 24–31.

[4] Y. Li, X. Chen, Y.L. Wu, et al., Experimental study on the effect of SiO_2 nanoparticle dispersion on the thermos physical properties of binary nitrate molten salt, Sol. Energy 183 (2019) 776–781.

[5] Y.T. Wu, Y. Li, N. Ren, C.F. Ma, Improving the thermal properties of NaNO3-KNO3 for concentrating solar power by adding additives, Sol. Energy Mater. Sol. Cells 160 (2017) 263–268.

[6] Y. T Wu, Y. Li, N. Ren, et al., Experimental study on the thermal stability of a new molten salt with low melting point for thermal energy storage applications, Sol. Energy Mater. Sol. Cell. 176 (2018) 181–189.

[7] B. Liu, Y.T. Wu, C.F. Ma, et al., Turbulent convective heat transfer with molten salt in a circular pipe, Int. Commun. Heat Mass Tran. 36 (9) (2009) 912–916.

[8] C. Chen, Y.T. Wu, S.T. Wang, et al., Experimental investigation on enhanced heat transfer in transversally corrugated tube with molten salt, Exp. Therm. Fluid Sci. 47 (2013) 108–116.

[9] S.Q. He, J.F. Lu, J. Ding, et al., Convective heat transfer of molten salt outside the tube bundle of heat exchanger, Exp. Therm. Fluid Sci. 59 (2014) 9–14.

[10] X.P. Yang, X.X. Yang, J. Ding, et al., Numerical simulation study on the heat transfer characteristics of the tube receiver of the solar thermal power tower, Appl. Energy 90 (1) (2012) 142–147.

[11] X. Chen, C. Wang, Y.T. Wu, et al., Numerical simulation of mixed convection heat transfer of molten salt in horizontal square tube with single surface heating, Appl. Therm. Eng. 104 (2016) 282–293.
[12] Y. Yang, M.H. Li, Z. Yang, et al., Numerical study on heat transfer characteristics of molten salt in annular channel with wire coil, Appl. Therm. Eng. 199 (2021), 117520.
[13] B.C. Du, Y.L. He, K. Wang, et al., Convective heat transfer of molten salt in the shell-and-tube heat exchanger with segmental baffles, Int. J. Heat Mass Tran. 113 (2017) 456–465.
[14] Y. Qiu, M.J. Li, W.Q. Wang, et al., An experimental study on the heat transfer performance of a prototype molten-salt rod baffle heat exchanger for concentrated solar power, Energy 156 (2018) 63–72.
[15] Y.L. He, Z.J. Zheng, B.C. Du, et al., Experimental investigation on turbulent heat transfer characteristics of molten salt in a shell-and-tube heat exchanger, Appl. Therm. Eng. 108 (2016) 1206–1213.
[16] X. Lu, G.P. Zhang, Y.T. Chen, Effect of geometrical parameters on flow and heat transfer performances in multi-stream spiral-wound tube heat exchangers, Appl. Therm. Eng. 89 (2015) 1104–1116.
[17] T.T. Wang, G.L. Ding, T. Ren, et al., A mathematical model of floating LNG spiral-wound tube heat exchangers under rolling conditions, Appl. Therm. Eng. 99 (2016) 959–969.
[18] S.M. Wang, G.P. Jian, X. Tong, et al., Effects of spacing bars on the performance of spiral-wound tube heat exchanger and the fitting of empirical correlations, Appl. Therm. Eng. 128 (2018) 1351–1358.
[19] G.P. Jian, S.M. Wang, L.J. Sun, et al., Numerical investigation on the application of elliptical tubes in a spiral-wound tube heat exchanger used in LNG plant, Int. J. Heat Mass Tran. 130 (2019) 333–341.
[20] A.M. Abolmaali, H. Afshin, Development of Nusselt number and friction factor correlations for the shell side of spiral-wound tube heat exchangers, Int. J. Therm. Sci. 139 (2019) 105–117.
[21] C.Z. Sun, Y.X. Li, J.L. Zhu, et al., Experimental tube-side pressure drop characteristics of FLNG spiral wound heat exchanger under sloshing conditions, Exp. Therm. Fluid Sci. 88 (2017) 194–201.
[22] X. Lu, X.P. Du, M. Zeng, et al., Shell-side thermal-hydraulic performances of multilayer spiral-wound tube heat exchangers under different wall thermal boundary conditions, Appl. Therm. Eng. 70 (2014) 1216–1227.
[23] G.P. Jian, S.M. Wang, J. Wen, Experimental study on the tube-side thermal-hydraulic performance of spiral wound heat exchangers, Int. J. Therm. Sci. 159 (2021), 106618.
[24] J.X. Wu, Q.H. Tian, X.Z. Sun, et al., Numerical simulation and experimental research on the comprehensive performance of the shell side of the spiral wound heat exchanger, Appl. Therm. Eng. 163 (2019), 114381.
[25] J. Fernandez-Seara, F.J. Uhıa, J. Sieres, et al., A general review of the Wilson plot method and its modifications to determine convection coefficients in heat exchange devices, Appl. Therm. Eng. 27 (2007) 2745–2757.
[26] C. C Zhang, S. l Shi, Y.W. Lu, et al., Heat discharging and natural convection heat transfer performance of coil heat exchanger in single molten salt tank, Appl. Therm. Eng. 166 (2020), 114689.
[27] C. C Zhang, Y.W. Lu, S. L Si, et al., Comparative research of heat discharging characteristic of single tank molten salt thermal energy storage system, Int. J. Therm. Sci. 161 (2021), 106704.
[28] C. C Zhang, Y.W. Lu, S. L Si, et al., Optimal research of annular baffle for heat-discharging performance of single thermal storage tank with molten salt, Int. J. Energy Res. 44 (7) (2020) 5582–5595.
[29] A. Shahsavar, M. Shahmohammadi, M. Arıcı, et al., Extensive investigation of the fluid inlet/outlet position effects on the performance of micro pin-fin heatsink through simulation, Energy Sources, Part A Recovery, Util. Environ. Eff. 44 (4) (2022) 9489–9505.
[30] H.R. Siddiqi, A. Qamar, R. Shaukat, et al., Heat transfer and pressure drop characteristics of ZnO/DIW based nanofluids in small diameter compact channels: an experimental study, Case Stud. Therm. Eng. 39 (2022), 102441.
[31] N.N. M Zawawi, W.H. Azmi, M.F. Ghazali, et al., Performance of air-conditioning system with different nanoparticle composition ratio of hybrid nanolubricant, Micromachines 13 (11) (2022) 1871.
[32] A. Rasheed, U. Allauddin, H.M. Ali, et al., Heat transfer and fluid flow characteristics investigation using detached ribs in an axisymmetric impinging jet flow, J. Therm. Anal. Calorim. 147 (2022) 14517–14537.
[33] J.W. Rose, Heat-transfer coefficients, Wilson plots and accuracy of thermal measurements, Exp. Therm. Fluid Sci. 28 (2004) 77–86.
[34] R.J. Moffat, Describing the uncertainties in experimental results, Exp. Therm. Fluid Sci. 1 (1988) 3–17.